



Coral-shaped Mn-CuS with hierarchical pores and crystalline defects for high-efficiency H₂O₂ production via electrocatalytic two-electron reduction

Ao Zhang ^{a,1}, Zhongqing Jiang ^{b,1}, Shaoda Zhang ^{c,1}, Penghua Lan ^d, Naihua Miao ^d, Weiheng Chen ^e, Ning Huang ^f, Xiaoning Tian ^g, Yangjie Liu ^h, Zhongyu Cai ^{a,*}

^a School of Instrumentation Science & Optoelectronic Engineering, School of Space and Environment, Beijing Advanced Innovation Center for Biomedical Engineering, Beihang University, Beijing 100191, China

^b Key Laboratory of Optical Field Manipulation of Zhejiang Province, Department of Physics, Zhejiang Sci-Tech University, Hangzhou 310018, Zhejiang, China

^c Shenzhen Cofoe Biotechnology Co., Ltd, Shenzhen 518108, Guangdong, China

^d School of Materials Science and Engineering, Beihang University, Beijing 100191, China

^e Vehicle Energy and Safety Laboratory, Department of Mechanical Engineering, Ningbo University of Technology, Ningbo 315336, China

^f State Key Laboratory of Silicon Materials, Department of Polymer Science and Engineering, Zhejiang University, Hangzhou 310027 China

^g Department of Chemical Engineering, Ningbo University of Technology, Ningbo 315016, Zhejiang, China

^h CAS Key Laboratory of Design and Assembly of Functional Nanostructures, and Fujian Provincial Key Laboratory of Nanomaterials, Fujian Institute of Research on the Structure of Matter, Chinese Academy of Sciences, Fuzhou, Fujian 350108, China



ARTICLE INFO

Keywords:

Coral-shaped Mn-CuS catalyst
Hydrogen peroxide production
Electrocatalysis
Hierarchical pores
Defects

ABSTRACT

We report the development of non-noble transition metal sulfide catalysts Mn-CuS-x for high-efficiency and selective H₂O₂ production. In this study, we synthesized Mn-CuS-x with coral-shaped hierarchical porous structure through one-pot hydrothermal reaction. The Mn-CuS-x possesses large specific surface area with plenty of crystalline defects via heteroatom doping of Mn. The Mn-CuS-x kinetically favored 2e⁻ pathway over 4e⁻ pathway, resulting in high selectivity (>92%) to H₂O₂ production and high H₂O₂ concentration (~24.5 mM at 0.6 V vs. RHE) within 3 h for the optimized Mn-CuS-2 catalysts (synthesized with a molar ratio of 1:3:8 (MnCl₂:4 H₂O: CuCl₂:2 H₂O: C₂H₅NS)). The Mn-CuS-2 showed excellent stability, indicating that the Mn-CuS electrocatalysts can simultaneously achieve both high stability and enhanced H₂O₂ production. Our first-principles calculations further confirmed that the heteroatom Mn doping to CuS thermodynamically makes the 2e⁻-ORR pathway more favorable. This study provides a green, low-cost, and efficient route to produce H₂O₂, which is very promising for generating chemicals and liquid fuels.

1. Introduction

Hydrogen peroxide (H₂O₂) is widely used as an eco-friendly oxidant in environmental treatment and chemical industry, and as a sustainable energy carrier in fuel cells, owing to its merits of high oxidation potential, ease of transportation and storage, and eco-friendly property [1–3]. The industrial mass production of H₂O₂ is mainly based on the well-established anthraquinone method, which suffers from a huge amount of organic waste generation and complex multistep post-processing treatment, resulting in low production efficiency [4]. Recently, the electrochemical synthesis of H₂O₂ based on the electricity-driven oxygen reduction reaction (ORR) has been reported as a promising method owing to its environment-friendly advantages [5].

Nevertheless, the yield of H₂O₂ is highly dependent on high-selective catalysis toward H₂O₂ production via a two-electron (2e⁻) transfer way, rather than the four-electron (4e⁻) pathway including O-O bond breaking to produce H₂O. In general, during the ORR process, the Gibbs binding free energy of *OOH intermediate determines both the selectivity and the catalytic activity of the electrocatalysts towards H₂O₂ production [6,7]. Therefore, it is a daunting challenge to develop an electrocatalyst with excellent catalytic activity and high selectivity towards H₂O₂ synchronously depressing the competitive reaction that leads to produce H₂O.

Nowadays, a large variety of electrocatalysts, such as noble metal/alloys, carbon-based materials, single-atom catalysts, transition metals, have been developed for selective and highly-efficient production of

* Corresponding author.

E-mail address: caizy@buaa.edu.cn (Z. Cai).

¹ These authors contributed equally.

H_2O_2 [8]. Noble metal/alloys, like Au, Ag, Hg, Pt, Pt-Hg, achieved high selectivity towards the production of H_2O_2 [9,10]. However, noble metal/alloys suffered from high cost and scarcity, which significantly limit their large-scale applications. Hence, researchers have devoted considerable efforts to noble metal-free electrocatalysts, including carbon-based materials, transition metal carbides and nitrides, single atom catalysts, MXenes, and molecular complexes [11–14]. Among these, carbon-based materials received the most research interest and were intensively investigated for the efficient production of H_2O_2 owing to their low cost, structure/property tunability, and eco-friendliness [12, 15,16]. Though great success has been achieved using carbon-based materials for H_2O_2 production, neither the reaction mechanisms nor the active centers of the electrocatalyst based on functional carbon materials are completely understood. Furthermore, the electrocatalytic activity still needs to be improved [12].

As a new two-dimensional material, MXene has a structure similar to graphene. Compared with graphene, MXene has better electrical conductivity and lower price [13,14]. Thus, MXenes are widely used in energy storage and catalysis. Wang et al. successfully constructed cobalt-dispersed nitrogen-doped carbon nanotubes supported on oxygen-terminated Nb_2CT_x MXenes (Co–NC/MXenes) for H_2O_2 production [17]. The assembled device with Co–NC/MXenes as cathode enables an accumulated H_2O_2 concentration of 4.8 wt% even under natural air diffusion. However, MXene is easy to oxidize in air, forming oxides on its surface, affecting its conductivity, and thus reducing its stability as a carrier of electrocatalyst. Therefore, it is an urgent to improve its chemical stability while ensuring its activity.

An alternative type of electrocatalyst is mainly based on transition metal materials. Transition metal-based materials have been regarded as one of promising electrocatalysts for 2e^- -ORR due to their excellent properties such as low cost, earth-abundance and high carrier mobility [11]. By using density functional theory (DFT) calculations, researchers have discovered that catalytic activity, in 2e^- -ORR toward H_2O_2 generation, of seven transition metal materials is higher than that of the PtHg in acid media [6,18]. Most transition metal electrocatalysts are based on transition metal oxides [19,20], or transition metal-nitrogen modified carbon [21,22]. Owing to their poor mass transfer, low electrical conductivity and electronic structure, most of these transition metal carbides and nitrides are designed as porous structure and loaded on functional carbon support to improve their electrocatalytic activity and durability [8].

Among non-noble transition metal materials, surprisingly, transition metal sulfides received less research attention though many of them show unique electrochemical properties [23]. For example, copper sulfide (CuS) is one kind of p-type semiconductors with a narrow band gap of ~ 2.1 eV, which is very promising for electrocatalyst owing to its high ionic conductivity and electrocatalytic activity comparing to its oxide counterparts [24–26]. CuS also possesses unique bandgap structure, which contains empty 3p-orbitals of sulfur and a large number of electrons, which is prone to capture electrons and promote the transport of electrons to react with electron donor molecules [27]. Unfortunately, CuS also faces several key challenges, including low electrical conductivity and limited active sites, which greatly hinder their electrochemical performance [28]. CuS is thus mainly used as electrocatalyst for the OER process rather than for the ORR process [29]. CuS-based electrocatalysts show a poor selectivity in the ORR process toward H_2O_2 production and are vulnerable for long-term operation.

To simultaneously improve the durability, catalytic activity and selectivity of CuS-based electrocatalysts, heteroatom-doping can be applied to develop potential electrocatalysts towards highly selective and efficient production of H_2O_2 [30]. In recent years, heteroatom-doping has been widely used as a promising method to modify the physicochemical properties of carbon-based nanomaterials and tune the interactions between internal atoms, thereby potentially improving their catalyst activity [31]. Ideally, heteroatom-doping can enhance catalytic activity of CuS-based electrocatalysts as well. The

metallic heteroatom-doping metallic phase into transition metal dichalcogenides has been proved to be able to improve the electronic conductivity [32,33]. We hypothesize that this strategy can also be used to improve the conductivity of CuS-based catalysts, and subsequently their stability. During this process, the metallic heteroatoms tend to enhance the conductivity of CuS when used as dopants into CuS by narrowing band gaps of CuS with manifesting metallic properties [34]. Furthermore, previous studies indicate that defects caused by heteroatom-doping can lead to the charge redistribution of the carbon-based electrocatalysts, which alter the mode of oxygen chemisorption to weaken the O–O bonding and promote the charge transfer during the ORR process [16,35]. In addition, similar to carbon-based electrocatalysts, proper surface functionalization or modification of CuS-based electrocatalysts can endow them with enhanced conductivity and increased defective edge sites, which may achieve enhanced selectivity toward the synthesis of H_2O_2 [15,35]. However, the general principle that governs their selectivity specifically towards H_2O_2 has not been fully elucidated. Thus, it remains a grand challenge to precisely tune the electrochemical properties of CuS-based catalysts in order to achieve high selectivity and high catalytic activity for H_2O_2 generation with good cyclic stability.

Here, we develop a non-noble transition metal sulfide Mn-CuS catalyst with hierarchical porous structure and defects derived from transition metal Mn doping by using a one-pot hydrothermal method. The resulting Mn-CuS-2 catalyst demonstrates an excellent selectivity (>92 –96% for Mn-CuS-x synthesized utilizing chemicals with a molar ratio of 1:3:8 (MnCl_2 ·4 H_2O : CuCl_2 ·2 H_2O : $\text{C}_2\text{H}_5\text{NS}$)) and enhanced electrocatalytic activity to H_2O_2 production via a 2e^- pathway and achieves a high yield of H_2O_2 with a concentration as high as ~ 24.5 mM at 0.6 V (vs. RHE) within 3 h, and the catalyst also shows a very good cycle stability. Owing to the simplicity of the synthesis protocol, environmental friendliness, and excellent cost-effectiveness, Mn-CuS-x is very promising for energy applications, which has enlightening significance for the design of other 2e^- -ORR catalysts and sheds light on many other energy-related heterogeneous electrochemical processes.

2. Experimental section

2.1. Materials and methods

CuCl_2 ·2 H_2O , MnCl_2 ·4 H_2O , thioacetamide, KOH, HCl, HClO_4 and ethylene glycol (analytical grade) were purchased from Sinopharm Chemical Reagent Co., Ltd. (China) and used as received. Cerium sulfate ($\text{Ce}(\text{SO}_4)_2$, 99.9% purity) was supplied by Aladdin Co. Ltd (Shanghai, China). All the chemicals are used as received.

The coral-shaped Mn-CuS composite nanosheets clusters were prepared through a one-pot hydrothermal method. In a typical process, CuCl_2 ·2 H_2O and MnCl_2 ·4 H_2O were first added into the mixture of ethylene glycol and deionized water (volume ratio of 3:1) under stirring for 20 min. To examine the effect of Mn amount on the structure and property of the final Mn-CuS catalysts, Mn-CuS-x composites containing different amounts of Mn were synthesized by controlling the molar ratio of Mn to Cu using the same method. Subsequently, thioacetamide (TAA) was added to the solution with magnetic stirring for 20 min. The solution was then transferred to a 100 mL stainless steel autoclave and heated under 180 °C for 3 h. Here, x represents the number of Mn-CuS samples. Detailed formulations of the Mn-CuS-x catalysts are shown in Table S1 (Electronic Supplementary Information, ESI).

2.2. Catalysts characterization

The morphologies of the samples were characterized by using a field-emission scanning electron microscope (FESEM) (S4800, Hitachi) at an operation voltage of 20.0 kV, and a field-emission transmission electron microscope (FETEM) (JEM 2010, JEOL, Japan) operated at 200 kV. The X-band continuous wave electron paramagnetic resonance (EPR)

measurement was conducted at 293 K on a Bruker A300-10-12 spectrometer at a frequency of 9.829972 GHz, which was used to investigate CuS and Mn-CuS-2. Specific surface areas and porosity of the samples were characterized with an automatic volumetric sorption analyzer (Quantachrome, Autosorb-IQ-MP). The phase analysis and crystal structure characterization of the synthesized materials were carried out by Bruker D8 Advance X-ray powder diffractometer, which used Cu K α radiation ($\lambda = 1.5406$ nm) and operated at voltage 40 kV, current 30 mA. The 20 angular regions between 5° and 85° were explored at a scan rate of 2° min $^{-1}$. The elemental compositions of the samples were determined by X-ray photoelectron spectroscopy (XPS) using a VG ESCALAB 250 spectrometer (Thermo Electron, UK) using an Al K α X-ray source (1486 eV). The nitrogen (N₂) physisorption of the samples was measured with Micrometrics ASAP 2000. The adsorbed water and other pollutant gases within all the samples must be removed by heating at 150 °C and vacuuming prior to the N₂ physisorption measurements. The Raman spectra were collected with XploRA PLUS (HORIBA, France). Inductively coupled plasma-atomic emission spectrometer (ICP-AES) measurement was carried out using Optima 7300 DV.

2.3. Electrochemical measurements

2.3.1. Rotating ring disk electrode (RRDE) test

The electrochemical performance of selective ORR was evaluated in a standard three-electrode system controlled by a potentiostat (CHI 760 C, CH Instrument, USA) with an RRDE setup. A Pt tablet and a saturated calomel electrode (SCE) were used as the counter-electrode and reference electrode, respectively. A pre-polished glassy carbon (GC) disc with Pt ring electrode (E7R9; Pine Instrument Company; 0.2475 cm 2 of disc area and 0.1866 cm 2 of ring area; 0.37 theoretical collection efficiency) was used as the working electrode.

The catalyst ink was prepared by dispersing 0.5 mg catalyst in a solution containing 0.99 mL of deionized water and 10 μ L of 5 wt% Nafion and sonicating for 10 min. The catalyst ink of 4.95 μ L was then casted on the surface of GC part of the RRDE and dried to form a uniform thin film, where the loading amount of electrode was 10 μ g cm $^{-2}$. Unless otherwise specified, the O₂-saturated 0.1 M KOH aqueous solution was used as an electrolyte for measurement, and the working electrode was rotating at 1600 rpm. (All measured potentials were converted into V vs. RHE (E_{RHE} = E_{SCE} + 0.059 V \times pH + 0.242 V)). A potential of 1.5 V was applied on the ring to collect the generated H₂O₂. The hydrogen peroxide selectivity (H₂O₂%) and number of electron transfers (n) and Faraday efficiency were calculated with the following Eqs. (1)–(3):

$$H_2O_2\% = 200 \times (I_r/N)/(I_d + I_r/N) \quad (1)$$

$$n = 4 \times (I_d/(I_d + I_r/N)) \quad (2)$$

$$FE(100) = \frac{100 \times \frac{I_r}{N}}{I_d} \quad (3)$$

where I_d is the disc current, I_r is the ring current, and N is the ring empirical collection efficiency (Fig. S1, ESI).

For comparison, the Koutecky-Levich (K-L) method was used to correct the mass-transportation limitations [36]. We obtained a linear plot between j_k^{-1} and $\omega^{-1/2}$ by varying the RRDE rotation rate. The kinetic current density (j_k) and electron transfer number (n) per oxygen molecule involved can be calculated from the intercept (j_k^{-1}) and slope (B^{-1}) of the linear plot (Eq. 4 and Eq. 5) [37]. the "j_k⁻¹" in Eq.(4) should be changed as "j_k⁻¹"

$$1/j_m = 1/j_l + 1/j_k = B^{-1}\omega^{-1/2} + j_k^{-1} \quad (4)$$

$$B = 0.62nFC_O D_O^{2/3} v^{-1/6} \quad (5)$$

where j_m is the measured total current density, j_l is the diffusion-limited

current density, j_k is the kinetic current density, ω is the electrode rotating rate, n is the overall number of transferred electrons during the ORR process, C_O and D_O is the concentration (solubility) (1.21×10^{-6} mol cm $^{-3}$) and diffusion coefficient (1.90×10^{-5} cm 2 s $^{-1}$) of O₂ in the 0.1 M KOH at 298 K respectively, v is kinematic viscosity of 0.1 M KOH (0.01 cm 2 s $^{-1}$). The expected shape of the linear sweep voltammetry curves (LSVs) should be S-shaped for an ideal catalyst. The steady maximum current value reached is the limiting diffusion current (I_l) when the electrode kinetics is very fast and the reaction rate is controlled by the diffusion of the reactants to the electrode surface. Therefore, the I_l can be calculated by the Levich method, where A is the area of the disk of RRDE (0.2475 cm 2) (Eq. 6) [38].

$$I_l = -0.62nFAD_O^{2/3} v^{-1/6} C_O \omega^{1/2} \quad (6)$$

2.3.2. Electrochemical direct synthesis of H₂O₂

The electrochemical ORR is performed in a custom-made H-type electrolytic cell with a Nafion membrane as the separator to quantify the amount of H₂O₂ (Fig. S2, ESI). The two-port chamber of the cell was filled with 50 mL O₂-saturated electrolyte with 10 mM ethylenediaminetetraacetic acid (EDTA). EDTA can be used as an inhibitor for H₂O₂ decomposition [39]. To remove oxides on the surface, the carbon paper was treated with 6 M HCl in advance, and then was used as the collector to test the electrochemical performance and stability of prepared electrode material during the process of H₂O₂ generation. The cathode was prepared by depositing Mn-CuS-x catalyst ink on a carbon paper with a dimension of 2 cm \times 2 cm (catalyst loading of 2 mg cm $^{-2}$). The electrolyte in the cathode compartment was bubbled with pure O₂ gas and stirred with a magnetic stirrer to guarantee the reactant can reach the electrode surface. The electrolyte in the cathode chamber is continuously bubbled with O₂ and is magnetically stirred to ensure that the O₂ can reach the electrode surface. In practice, the device is often operated under a constant current or potential. Therefore, we controlled the constant potential of H₂O₂ production and catalyst durability test at –0.65 V (vs. SCE).

2.3.3. H₂O₂ concentration measurement

The H₂O₂ concentration can be measured by a traditional cerium sulfate Ce(SO₄)₂ titration method [40,41]. In the presence of H₂O₂, yellow Ce⁴⁺ solution can be reduced to colorless Ce³⁺, and the reaction is shown as follows (Eq. 7):

$$2Ce(SO_4)_2 + H_2O_2 \rightarrow Ce_2(SO_4)_3 + H_2SO_4 + O_2 \quad (7)$$

The Ce⁴⁺ can be measured by ultraviolet-visible infrared (UV-Vis-NIR) spectroscopy (~318 nm). Therefore, we prepared 1 mM of Ce (SO₄)₂ solution by dissolving 33.2 mg Ce(SO₄)₂ salts in 100 mL 0.5 M sulfuric acid solution. To obtain the calibration curve, a series of H₂O₂ solutions at different concentrations were titrated with the Ce(SO₄)₂ solution and measured using UV-Vis-NIR. Based on the linear relationship between the absorption spectra changes (Δ Abs) of Ce⁴⁺ (concentration: 0.1–1.9 mM) and the H₂O₂ concentration, the calibration curve can be obtained. The H₂O₂ concentrations of the samples generated can be determined (Fig. S3, ESI).

2.4. DFT calculations

All the calculations were performed using a plane-wave basis projector-augmented wave method [42] as implemented in the Vienna ab initio Simulation Package (VASP) [43], using the generalized gradient approximation (GGA) with the Perdew-Burke-Ernzerhof (PBE) parametrization [44]. The density functional dispersion correction (D3-Grimme) [45] was adopted for the van der Waals (vdW) interactions. A kinetic energy cutoff of 420 eV was set for plane-wave basis. The convergence criterion of total energy was 10 $^{-5}$ eV in self-consistent calculations and that of residual forces on atoms was 0.05 eV Å $^{-1}$ for geometry optimization. Uniform k-grids with a

reciprocal spacing of 0.04 were generated to sample the Brillouin zones. A vacuum spacing of 20 Å along the z axis was applied to avoid interactions between adjacent slabs. Single-atom Mn replaced the one of the f-site of Cu in the CuS primitive cell, since the four f-sites of each primitive cell was equivalent, a $2 \times 2 \times 1$ supercell with Mn replaced f-site of each CuS primitive cell was chosen as the conventional cell. To further study the interaction mechanism between the adsorbate and substrate, the charge density difference $\Delta\rho$ is calculated (Eq. 7):

$$\Delta\rho = \rho_{\text{tot}} - \rho_{\text{Mn}} - \rho_{\text{CuS}} \quad (8)$$

where ρ_{tot} , ρ_{Mn} and ρ_{CuS} are the charge density of the whole slab structure and separate parts, respectively. VESTA was used to visualize coordinate data and electron localization function (ELF). The crystal orbital Hamilton population (COHP) [46,47] was performed using the program LOBSTER [48] to analyze the Mn-OOH interactions.

3. Results and discussion

3.1. Physicochemical characterizations

The SEM images in Fig. 1 show the morphologies of as-prepared pure CuS and Mn-CuS array. As shown in Fig. 1a, the synthesized CuS sample is regular plate-like array with an average length of ~ 200 nm and an average thickness of ~ 40 nm. Compared to the pure CuS, due to Mn-doping, the Mn-CuS-1 nanoplates aggregate (Fig. 1b) and form coral-shaped array with rough surface. With increasing of Mn content, the plate-like tentacles of irregular coral-shaped Mn-CuS-x become thinner and sharper, and a sheet-like tentacle structure is formed inside Mn-CuS-2 (Fig. 1c). When $x = 3$ (Fig. 1d), the irregular coral-shaped arrays are disseminated randomly into nanosheet clusters inside Mn-CuS-3. By increasing the Mn content to $x = 4$, the nanosheet clusters further aggregate into three-dimensional (3D) flower-like Mn-CuS-4, which are obvious as shown in Fig. 1e. When the content of Mn is increased to $x = 5$ in Fig. 1f, two phases of Mn-CuS and MnS appear in the SEM images at the same time. The Mn-CuS shows a plate-like structure while MnS array shows cubic-like microstructure. This indicates that excessive Mn leads to the formation of additional MnS phase instead of Mn-CuS, which is further confirmed by the SEM image of pure MnS (Fig. S4, ESI). Table S2 shows the atomic content of Mn in the resulting Mn-CuS-x

sample deriving from ICP-AES. From Fig. 1a to f, we observe the effect of Mn doping content on the morphology of the Mn-CuS. Owing to the doping of Mn atoms, both the size difference and tendency of aggregation change gradually. Both factors can lead to the formation of a larger specific surface area in the Mn-CuS. The morphology of Mn-CuS is controllable and thus we can optimize the experimental parameters to achieve the best performance. It should be noted that, since the solubility of CuS is much lower than that of MnS ($K_{\text{sp}}(\text{CuS}) = 1.27 \times 10^{-36} < K_{\text{sp}}(\text{MnS}) = 1.4 \times 10^{-15}$), CuS is more easily generated, which also leads to an upper limit for the doping amount of Mn [49].

The nanostructures of these samples were further investigated using TEM, and the results are consistent with SEM results both in morphology and size of Mn-CuS. Fig. S5a-c (ESI) demonstrates the nanoplate-like morphology of CuS, where two vertical lattice spacings of 0.19 and 0.28 nm correspond to the (170) and (130) plane of CuS, respectively [26]. Typical selected area electron diffraction (SAED) confirms that the resulting CuS is assigned to be a hexagonal phase (the inset of Fig. S5c, ESI). Due to its best electrocatalytic activity among the Mn-CuS-x samples (see below), Mn-CuS-2 was selected as the representative sample for detailed further characterization. Fig. 2a shows the overview of the coral-shaped Mn-CuS-2. From the HRTEM images of Mn-CuS-2 (Fig. 2b-c), the microstructure of the hierarchical porous nanosheets can be easily observed with evenly distributed pores, which are disordered in the tentacles of the coral. The magnified high-resolution scanning transmission electron microscopy (HRSTEM) image of the edge site for Mn-CuS-2 is shown in Fig. 2d. The lattice spacing of 0.33 and 0.28 nm corresponds to the (110) and (130) plane of CuS, respectively (JCPDS No. 06-0464) [50]. It is well known that both the pore size distribution and surface area of electroactive materials play a key role in electrocatalytic applications. Hence, N_2 adsorption-desorption measurements were conducted to further investigate the specific pore size distribution and surface area of the CuS and Mn-CuS-x. As shown in Fig. 2e, the isotherms of Mn-CuS-x show a typical I-V curve with H3-type hysteresis loops, indicating the formation of mesopores and macropores structure ($P/P_0 > 0.5$). The pore size distribution mainly ranges from 2 to 60 nm for Mn-CuS-x (Fig. 2e, inset), which can be attributed to the introduction of Mn and the formation of hierarchical porous structure of coral-shaped Mn-CuS. This is consistent with the TEM images. The physicochemical and electrochemical properties of the CuS and the Mn-CuS-x catalysts are summarized in Table 1. In addition, among all

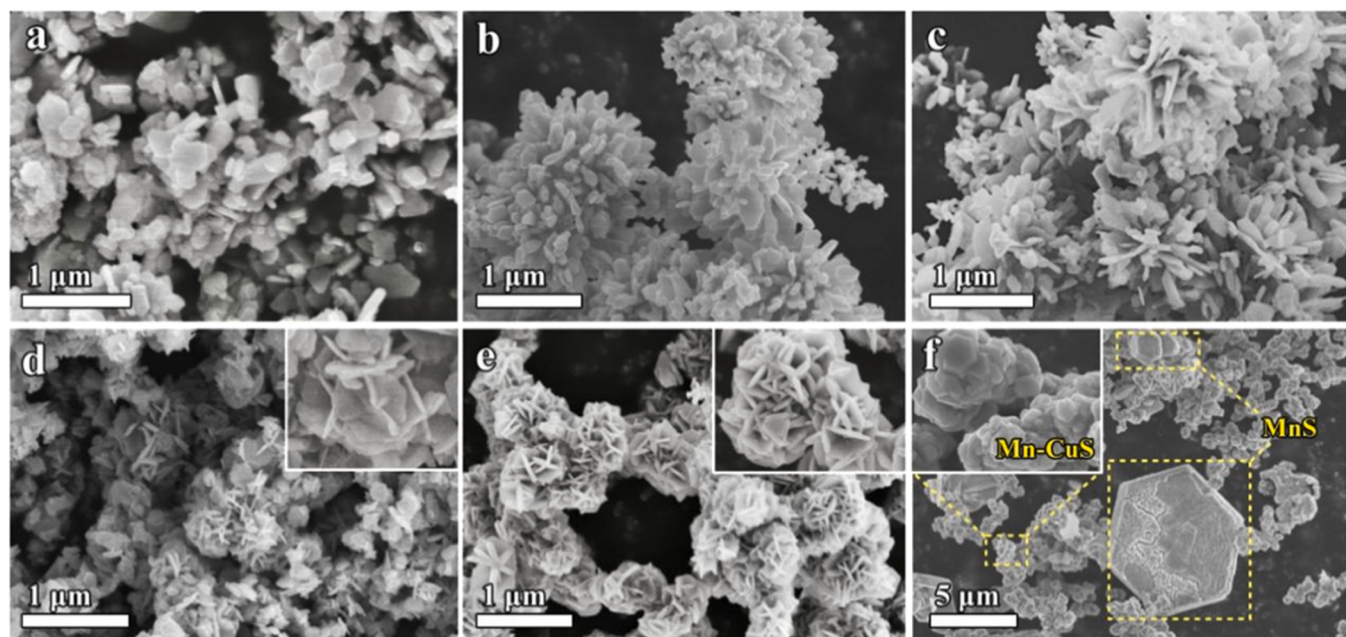


Fig. 1. SEM images of (a) CuS; (b) Mn-CuS-1; (c) Mn-CuS-2; (d) Mn-CuS-3; (e) Mn-CuS-4; and (f) Mn-CuS-5.

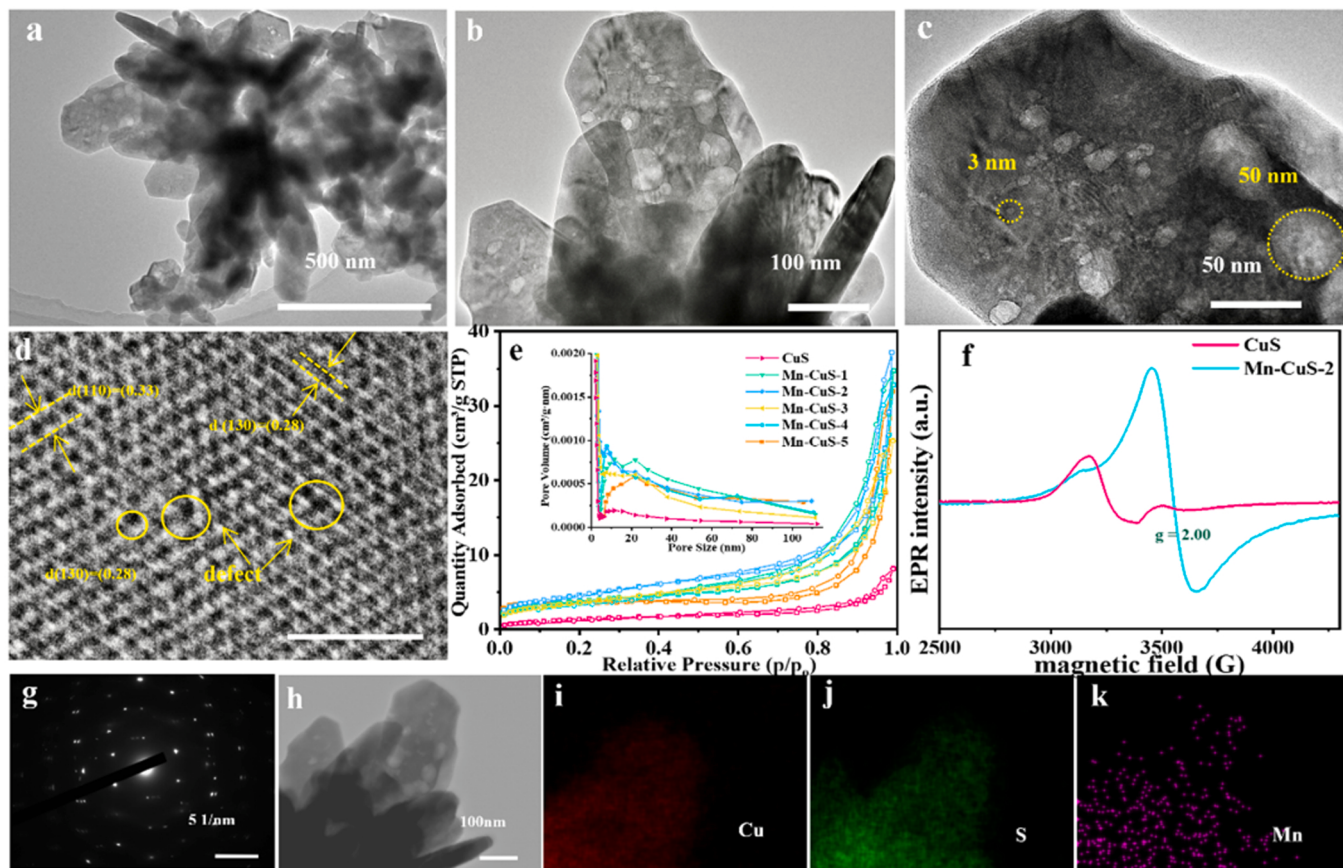


Fig. 2. (a-c) High-resolution STEM image of Mn-CuS-2; (d) Magnified high-resolution STEM images of Mn-CuS-2; (e) N_2 sorption isotherms of the six samples, the inset is the corresponding pore size distribution profile; (f) EPR spectra of CuS and Mn-CuS-2; (g) SAED pattern of Mn-CuS-2; (h-k) Element mapping images for Mn-CuS-2.

Table 1
Summary of the physiochemical and electrochemical properties of the CuS and the Mn-CuS-x catalysts.

Samples	BET surface area ($m^2 g^{-1}$)	Total pore volume ($cm^3 g^{-1}$)	H_2O_2 selectivity at 0.73 V (%)	Faraday efficiency at 0.73 V	Electron transfer number at 0.5 V	H_2O_2 current at 0.5 V
CuS	5.44	0.013	68.3	51.8	3.29	0.063
Mn-CuS-1	14.87	0.049	82.0	69.5	2.29	0.316
Mn-CuS-2	17.13	0.057	96.5	93.2	2.13	0.450
Mn-CuS-3	12.22	0.051	80.3	67.0	2.26	0.339
Mn-CuS-4	13.62	0.054	89.0	80.1	2.53	0.243
Mn-CuS-5	13.59	0.039	94.8	90.2	2.66	0.168

samples, Mn-CuS-2 with a hierarchical structure exhibits a larger surface area ($17.13 m^2 g^{-1}$) and a bigger total pore volume ($0.057 cm^3 g^{-1}$). This particular morphology with a hierarchical macro-mesoporous structure and improved specific surface area can provide more potential reaction sites and diffusion channels, which can facilitate mass transfer and surface chemical reaction to achieve enhanced catalytic activity [51].

Furthermore, some defect sites can also be found in Fig. 2d. The surface defect states on metal sulfides/oxides play an extremely important role in enhancing the chemisorption of the analyte molecules [52]. The existence of anion vacancies could also introduce more active sites for producing H_2O_2 as well as regulating the electronic structure and interface properties of Mn-CuS-2 [53]. To verify the category and the quantity of the surface defects as well as vacancy features, an EPR

spectrometer was used to further analyze the features of the samples. As can be seen in Fig. 2f, both samples show signals at $g = 2.00$, which is caused by the charge state of anion vacancies in the Transition Metal Sulfide (TMS) material, and S vacancies increase significantly in the sample after Mn doping. Meanwhile, we observed the paramagnetic signal of Mn ions remarkably broadened upon the introduction of alien electrons in Mn-doped CuS (acting as a new paramagnetic center). Hence, the interactions between Mn ion and alien electrons, is consistent with previous report [54]. The above results indicate that the alloying reaction is a feasible path to introduce anion vacancies into TMS materials, which may be caused by the increased disorder and distortion in the crystal structure when two anions coexist in the lattice [55]. It can be seen from the SAED pattern (Fig. 2g) that the Mn doping does not change the crystalline structure. Both the high-angle annular dark-field

scanning TEM (HAADF-STEM) and element mapping images demonstrate the homogenous distributions of Mn, Cu, and S in Mn-CuS (Fig. 2h-k). The morphologies of other synthesized samples of Mn-CuS-x ($n = 1, 3, 4, 5$) were also investigated by using TEM, HRTEM and mapping, as profiled in Fig. S5–6 (ESI).

The crystallographic structures of all Mn-CuS-x and pure CuS materials were measured with X-ray diffraction (XRD) patterns, which are shown in Fig. 3a. As can be seen, the pure CuS shows high crystallinity, whose diffraction patterns are consistent with the phase of covellite CuS (JCPDS#06–0464). With the incorporation of Mn atoms, the crystallinity of the Mn-CuS-x samples decreases, which can be ascribed to the increased disorder and distortion in the crystalline structure during the alloying reaction. The major diffraction peaks shift a little to the lower angle as the Mn content increases. This is mainly due to the gradual expanding of the unit cells upon the substitution of Cu atoms by the slightly bigger Mn atoms, implying the blending of Cu and Mn at the atomic level [56]. Several new diffraction peaks at 20 of 27.6°, 29.4°, 45.7°, 49.5° and 54.1° can be seen in Mn-CuS-5, which are attributed to the diffraction peaks of γ -MnS (Fig. S7, ESI) [57].

Raman spectra were collected to gain further insight into the structural changes in Mn-CuS-x during the alloying process (Fig. 3b). In the Raman spectrum of the as-synthesized sample, the strong and characteristic peak at $\sim 468 \text{ cm}^{-1}$ can be attributed to the stretching mode (A_{1g} symmetry) of the S–S bond, according to the S_2 groups of the acknowledged crystal structure of CuS [58,59]. The weak peak at $\sim 262 \text{ cm}^{-1}$ can be attributed to the stretching vibrational S mode of the covalent S–S bonds and the Cu–S bond vibration, respectively. Both

agree well with the covellite structure of CuS [58]. After doping with Mn atoms, the Mn–S-related modes start to appear in the range of 600–700 cm^{-1} for Mn-CuS-4 and Mn-CuS-5, and gain increased intensity as the amount of Mn increases [60].

The surface compositions of Mn-CuS with different Mn contents were analyzed using XPS. The detailed manganese dopant content on the surface of the Mn-CuS catalysts were also determined (Table S3, ESI). Fig. 3c shows the high-resolution Cu 2p XPS spectra of Mn-CuS catalysts. The asymmetric Cu 2p peaks can be contributed to the different chemical states of Cu in Mn-CuS-2. The peak separation of 20.0 eV between Cu 2p3/2 and Cu 2p1/2 located at 932.7 eV and 952.7 eV, respectively, indicates that copper is present in the form of monovalent Cu^+ [61,62]. The peaks of 2p3/2 and 2p1/2 located at 934.9 eV and 954.9 eV, respectively, are attributed to the spin-orbit splitting of the bivalent Cu^{2+} . The Cu 2p3/2 peaks of Mn-CuS-x red-shifted to a lower binding energy compared to that of CuS nanoplates (932.2 eV), which may be attributed to the increase of Cu^+ content [58,63]. Since the oxidation state of Cu slightly decreases with the increase of Mn precursor, it can be reasonably assumed that the CuS lattice is more likely to be destroyed when introducing more Mn. The high-resolution XPS spectra of Mn was surveyed in Fig. 3d. The Mn spectra can be deconvoluted into two peaks of Mn 2p1/2 ($\sim 649 \text{ eV}$) and Mn 2p3/2 ($\sim 641 \text{ eV}$) [49,64], which are indicative of the presence of Mn^{2+} . In particular, the predominant presence of Mn^{2+} suggests that cation exchange with Cu^{2+} occurred. With the increase of manganese content, a new peak appears in Mn-CuS-5, which is mainly attributed to Mn 2p1/2 of MnS. This is consistent with high-resolution XPS spectra of Mn 2p in pure MnS in

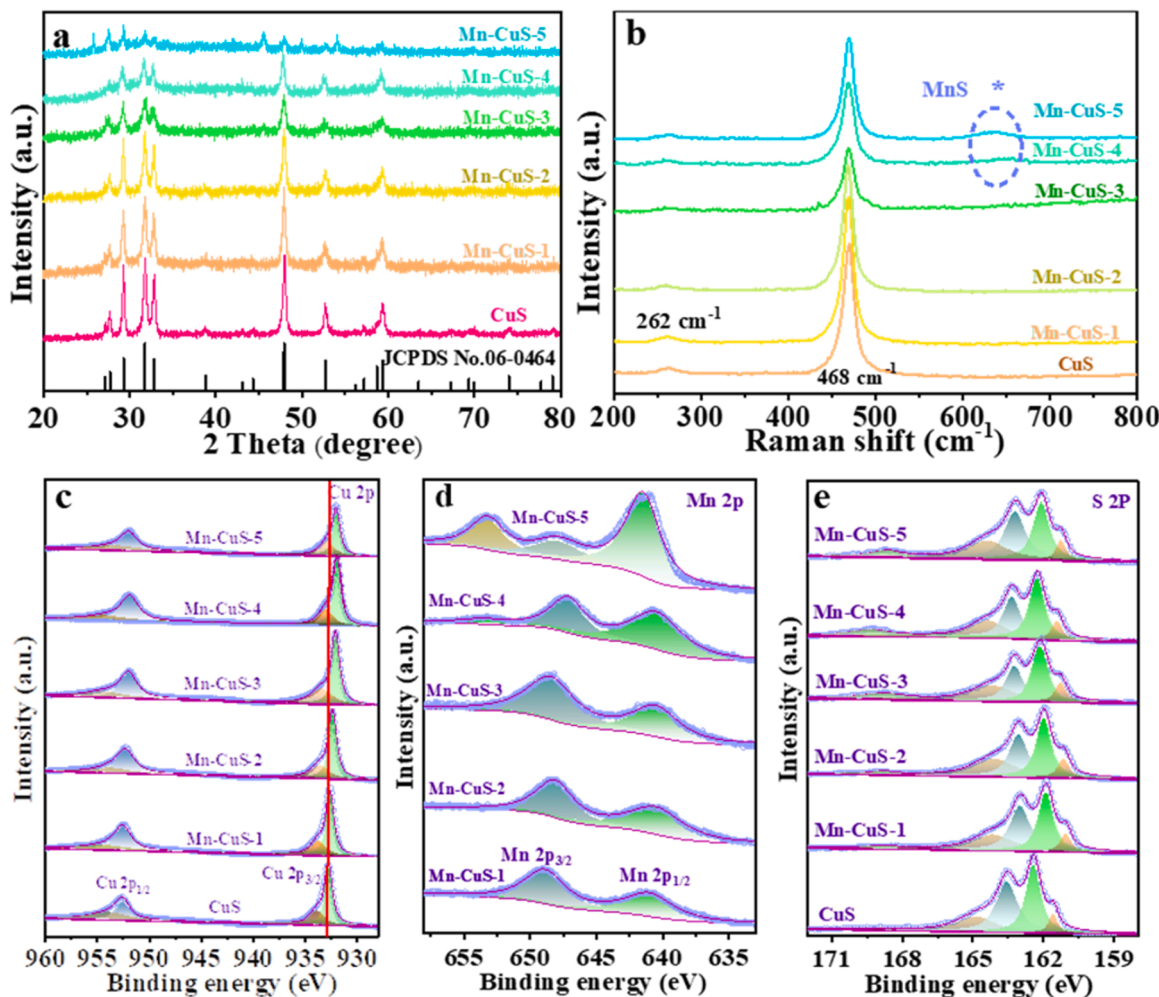


Fig. 3. (a) XRD patterns; (b) Raman for all the as-prepared Mn-CuS samples; (c-e) XPS of (c) Cu, (d) Mn and (e) S for all the as-prepared Mn-CuS samples.

Fig. S8 (ESI). The peak at 649 eV is attributed to Mn 2p1/2 of Mn-CuS-2. The above results are consistent with SEM and TEM images. The Mn 2p peaks of Mn-CuS red-shifted to a lower binding energy with the increase of Mn content, which can be attributed to the existence of Cu. **Fig. 3e** shows the high-resolution XPS spectra of S 2p. The S 2p peaks at 163.6 eV belongs to the S^{2-} , and peaks at 161.5 eV, 162 eV and 168 eV belong to the M–S (Metal-sulfur).

3.2. Electrocathodic ORR to H_2O_2 on RRDE

Nowadays, many transition metals, such as Fe, Ni, Cd, have been doped into CuS which can modulate the electronic structure, tune the interactions between metal and S, and form active metal-CuS sites [29, 65,66]. This method is believed to be able to greatly enhance the reaction kinetics and electrocatalytic activity of CuS-based electrocatalysts. In this study, ORR kinetics can be carried out via either $2e^-$ or $4e^-$ pathway (**Fig. S9**, ESI), and its selectivity depends on the tendency to break the O–O bond during the ORR process. The formation of H_2O_2 is qualified by RRDE (1600 rpm) in an 0.1 M oxygen-saturated KOH electrolyte. To oxidize the H_2O_2 only formed on the disk electrode and avoid other ORR currents of the ring electrode, the ring electrode potential is constant at 1.5 V. The loading amount of the disk electrode was set as $10 \mu\text{g cm}^{-2}$ during the whole experiment process (**Fig. S10**, ESI). In this section, the $2e^-$ -ORR activities of the as-synthesized catalysts were evaluated by the RRDE method. Compared with pure CuS, a larger ring current was observed using Mn-CuS as the catalyst (**Fig. 4a**), indicating the high selectivity and Faraday efficiency for the production of H_2O_2 . The selectivity and Faraday efficiency for the production of H_2O_2 was calculated and shown in **Fig. 4b**, **Fig. S11**(ESI) and **Table 1**. Among all of the samples, the Mn-CuS-2 shows the highest selectivity for H_2O_2 generation over the entire current region. The Mn doping could improve

$2e^-$ -ORR activity of CuS, especially, the selectivity of H_2O_2 reaches $> 92\%$ (FE $> 85\%$) for the Cu-MnS-2 (selectivity of H_2O_2 and Faraday efficiency $> 96\%$ and $> 93\%$ at 0.73 V, respectively), which can be attributed to the formation of hierarchical pores structure and the defects introduced by Mn doping. **Fig. 4c** compares the H_2O_2 current (ring current) using CuS and Mn-CuS as catalysts at a constant voltage of 0.5 V. It is apparent that the H_2O_2 current generated by Mn-CuS catalysts are much higher than that of pure CuS, indicating that Mn-CuS catalysts have excellent activity and selectivity towards H_2O_2 production. We calculated the number of electrons transferred on the catalyst, which shows the ORR process of Mn-CuS-2 is a typical $2e^-$ process towards H_2O_2 (**Fig. S12**, ESI). The semicircle of the electrochemical impedance spectroscopy (EIS) curve represents the charge transfer resistance (RCT) of the catalysts. As can be seen from **Fig. 4d**, the RCT of pure CuS is much larger than that of Mn-CuS, indicating that the electrochemical kinetics in the catalytic process will be significantly improved with the doping of Mn. The Mn-CuS-5 catalyst shows the largest RCT among the Mn-CuS-x catalysts, and even larger than pure CuS, implying that the presence of pure MnS severely reduces the conductivity of the material, thereby increasing the electrochemical kinetics. Moreover, the obtained Mn-CuS-2 catalyst is stable for the H_2O_2 production process. After 500 LSVs cycles, both the current drop and selectivity of H_2O_2 drop are less than 5% (**Fig. 4e**).

To understand the ORR electron transfer kinetics in depth, the LSVs of Mn-CuS-2 was investigated by changing the electrode rotation rate under the same experimental conditions. As shown in **Fig. 5a**, the measured current intensity increases with the electrode rotation rate. **Fig. 5b** shows that, under various electrode potentials, there is a linear relationship between j^{-1} and $\omega^{-0.5}$ for all electrodes. The kinetic current density of the Mn-CuS-2 catalysts for H_2O_2 production was calculated to be $2.6 \pm 0.2 \text{ mA cm}^{-2}$ (at 0.4 V), which shows its superior H_2O_2

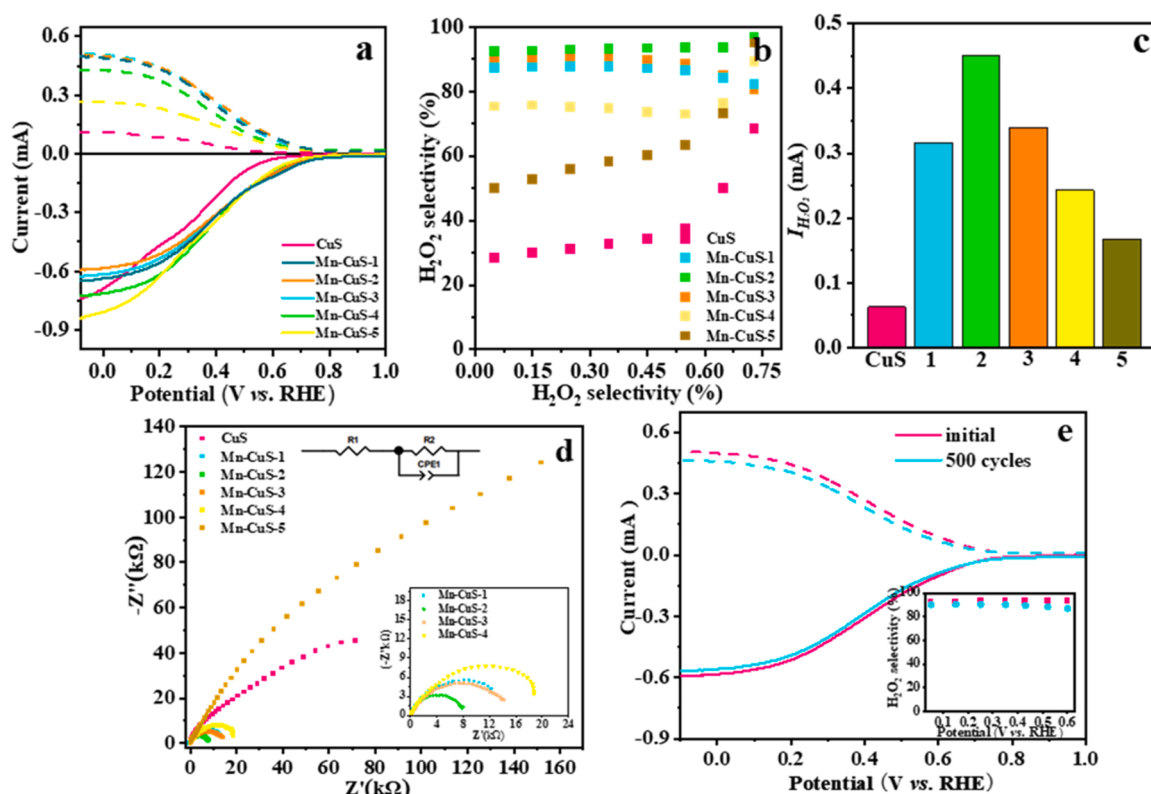


Fig. 4. (a) Comparison of ORR performance at 1600 rpm (solid lines) and the simultaneous H_2O_2 detection current at the ring electrode (dashed lines) for CuS and Mn-CuS catalysts. The disk potential was scanned at 10 mV s^{-1} and the ring potential was constant at 1.5 V vs. RHE. (N = 37.3%). (b) The calculated H_2O_2 selectivity at various potentials from RRDE data. (c) Comparison of H_2O_2 current (at 0.5 V) for CuS and Mn-CuS. (d) EIS for CuS and all as-prepared Mn-CuS samples. (e) The polarization curves of Mn-CuS-2 before and after durability test for 500 LSVs cycles. The inset is the selectivity of the catalyst.

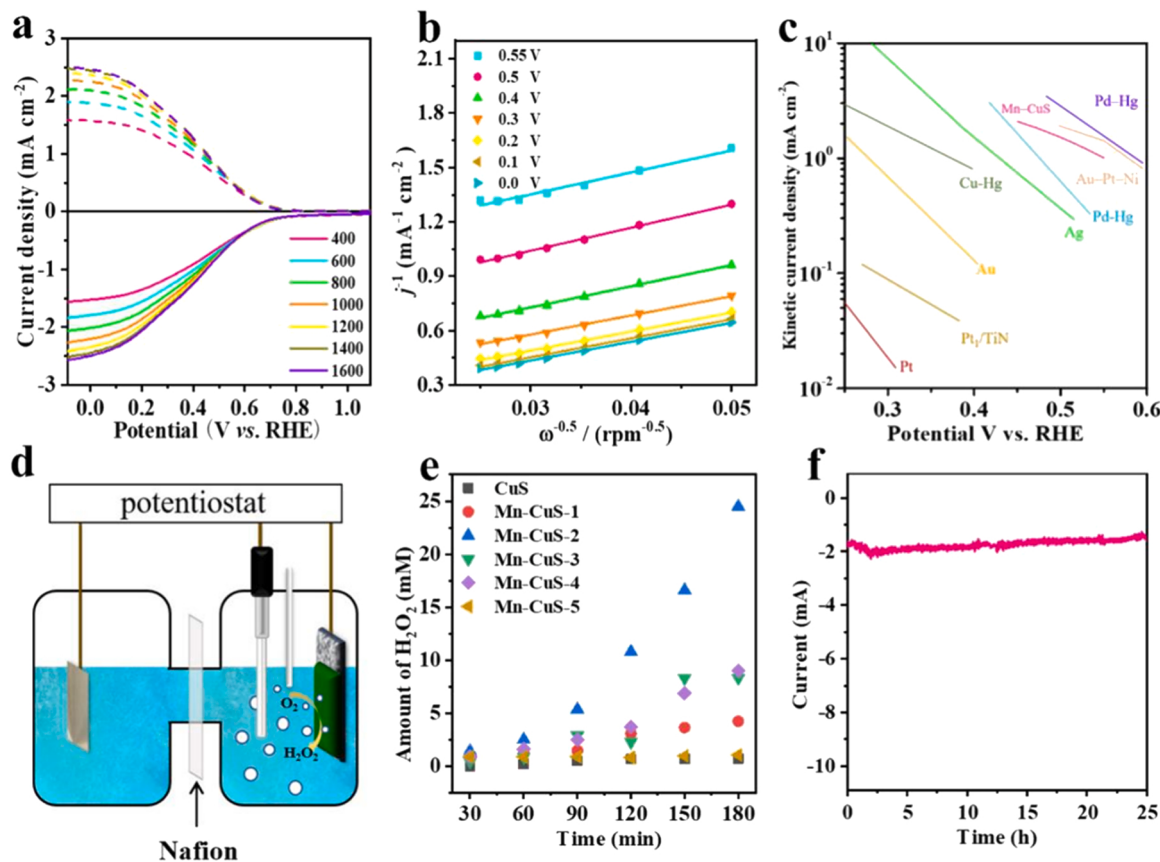


Fig. 5. (a) LSVs curve of Mn-CuS-2 electrode measured with different rotating rates; (b) K-L plots at different potentials calculated from the LSVs with different rotating rates; (c) Kinetic current density of Mn-CuS-2 and other metal materials [7,9]. (d) The electrochemical device used for the electrochemical production of H₂O₂. (e) The amount of generated H₂O₂ along with reaction time at a cell output voltage of 0.6 V. (f) Chronoamperometry stability test of Mn-CuS-2 (at 0.6 V in 0.1 M KOH).

generation activity compared with other materials (Fig. 5c). Meanwhile, the mass activity of Mn-CuS-2 catalysts during the ORR towards H₂O₂ generation reaches $169 \pm 3 \text{ A g}^{-1}$ (at 0.4 V, 1600 rpm) (Fig. S13, ESI). Both the kinetic current density and mass activity indicate that Mn-CuS-2 catalysts possess very good catalytic activity compared with other metal catalysts [7,9]. To further explore the performance of the catalysts, we successively used 0.1 M PBS and 0.1 M HClO₄ as the electrolyte solution. Obviously, the Mn-CuS catalyst still shows considerable H₂O₂ current and selectivity (~70%) in neutral solution (0.1 M PBS, pH = 7.1). However, in acidic solution (0.1 M HClO₄, pH = 2), it does not show good ORR activity towards H₂O₂ production. No matter in which of the above electrolytes, the doping of Mn plays a crucial role in the improvement of the catalytic ability of CuS (Fig. S14, ESI).

3.3. Electrocathodic ORR to H₂O₂ from the H-type cell

To evaluate the amount of H₂O₂ in the scale-up production, we designed a customized H-type electrolytic cell as a simulation device and embedded with the catalyst-loaded carbon paper for testing (Fig. 5d). We examined the effect of reaction temperature on H₂O₂ selectivity in the alkaline electrolyte. The overall ORR kinetics and H₂O₂ selectivity increase when the reaction temperature increases, which is consistent with previous studies (Fig. S15a, ESI) [41]. However, high accumulation of H₂O₂ cannot be achieved since the generated H₂O₂ usually decomposes faster at high temperature (Fig. S15b, ESI). Therefore, we investigated decomposition experiments of H₂O₂ at different H₂O₂ concentrations in electrolyte solutions and found that H₂O₂ is more easily decomposed as the initial H₂O₂ increases (Fig. S16, ESI). Meanwhile, the reduction current of H₂O₂ on the prepared CuS and Mn-CuS

catalysts was recorded, and it was found that CuS has the largest reduction current, indicating that H₂O₂ may be reduced to H₂O (Fig. S17, ESI). Therefore, we chose to carry out the electrochemical H₂O₂ production using Mn-CuS catalyst at room temperature (~25 °C) and using EDTA as inhibitor. The Mn-CuS-2 showed a very high H₂O₂ yield, reaching 24.48 mM within 3 h (at 0.6 V) (Fig. 5e). Compared with other materials, Mn-CuS-2 catalysts achieved considerable high H₂O₂ output [67,68], which proved the feasibility of electrochemical production of H₂O₂ with Mn-CuS-2 catalyst. In addition, it can be seen from Fig. 5f that the Mn-CuS-2 catalyst can remain stable under alkaline conditions to produce H₂O₂ for a long time, and can maintain 93.4% original activity within 25 h at 0.60 V. After the test of stability, the chemical configurations are well preserved and there is negligible structural change as confirmed using both the SEM microscopy and XPS spectra analysis (Fig. S18, ESI). In this study, coral-shaped Mn-CuS-2 showed the best electrocatalytic activity, indicating that the doping content of Mn reached its optimum. This can be attributed to the relatively large specific surface area of coral-shaped Mn-CuS-2 with thin tentacles. The catalytic effect of the material is significantly reduced upon the pure MnS phase appears, indicating that the improvement of the material performance is mainly due to the bimetallic sulfide Mn-CuS formed by Mn doping. For comparison, the composite material MnS/CuS is synthesized for H₂O₂ production (Fig. S19, ESI), whose selectivity and yield are far inferior to Mn-CuS-2 (Fig. S20, ESI).

3.4. Mechanistic understanding for O₂ activation

When an electron-rich species was adsorbed near the catalyst site, the charge state of the latter became more positive and ΔG_{OOH^*}

increased [41], which is favorable for electrochemical H_2O_2 production. Similarly, when an electron-poor metal species, such as Mn, substituted the Cu, the charge state of the atoms (metal) in the catalyst site also will become more positive and ΔG_{OOH^*} will increase. Table S4 (ESI) and Fig. 6a show that the Bader charge of the atoms (electron-poor metal species, i.e., Mn) in the catalyst site became more positive about 0.3e⁻ since the electron loss. Consequently, doping Mn in CuS catalyst is a rational strategy to produce H_2O_2 . In accordance with our expectation, the charge state of the atoms (metal) in the catalyst site become more positive and ΔG_{OOH^*} increase (Fig. 6b). An increased ELF between Mn atoms and their neighbor atoms suggests the enhancement of the delocalization of electrons and the interaction between these two kinds of atoms (Fig. 6c and Fig.S21), which agrees well with the above discussion in Fig. 6a. There was no conspicuous change in the bonding mode of the bulk crystal after doping Mn. It can be seen that the metal-S bonds are ionic. Fig. 6d shows that Mn-OOH bonding falls into antibonding regions around the Fermi level because the delocalized electrons filled the antibonding energy levels (blue areas under the Fermi level). Hence the bond order was decreased and the Mn-OOH bonding was easy to cleavage. That is the reason why OOH^* was hopeful to be obtained. Calculations show that the doping of Mn to CuS thermodynamically makes the 2e⁻-ORR pathway beneficial to the 4e⁻-ORR, resulting in high selectivity for H_2O_2 production. The corresponding reaction mechanism is proposed in Fig. 6e.

4. Conclusion

We developed a novel bimetallic sulfide Mn-CuS, which formed by a manganese doping strategy. This method not only changed the configuration of the surrounding atoms of the CuS catalyst, but also introduced

a coral-shaped hierarchical porous structure to achieve a substantial increase in specific surface area and introduced a large number of crystalline defects, which make the 2e⁻ pathway is kinetically favored over 4e⁻ pathway. This 2e⁻ pathway resulted in high selectivity (>92%) to H_2O_2 production and the H_2O_2 concentration as high as ~24.5 mM at 0.6 V (vs. RHE) within 3 h for the optimized Mn-CuS-2 catalysts (synthesized with chemicals in a molar ratio of 1:3:8 (MnCl₂·4 H₂O: CuCl₂·2 H₂O: C₂H₅NS)). The optimized Mn-CuS-2 catalyst showed the best stability (without any noticeable decay as long as 25 h), which indicates that Mn-CuS can simultaneously achieve high stability and significant enhancement of H_2O_2 production. The DFT calculation further confirmed the doping of Mn thermodynamically makes the 2e⁻-ORR pathway more favorable, resulting in the excellent selectivity for H_2O_2 production. This study provides a green, low-cost and efficient route to produce H_2O_2 , which demonstrates promising generation of chemical and liquid fuel for future applications.

CRediT authorship contribution statement

Ao Zhang: Conceptualization, Methodology, Investigation, Writing – original Draft, Visualization. **Zhongqing Jiang:** Methodology, Formal analysis, Writing – original draft, Writing – review & editing, Funding acquisition. **Shaoda Zhang:** Methodology, Formal analysis, Resources, Validation, Writing – original draft, Writing – review & editing. **Penghua Lan:** Conceptualization, Methodology, Investigation, Software, Writing – original draft, Writing – review & editing. **Naihua Miao:** Conceptualization, Methodology, Writing – original draft, Writing – review & editing, Supervision, Funding acquisition. **Weiheng Chen:** Formal analysis, Writing – review & editing. **Ning Huang:** Resources, Writing – original draft, Funding acquisition. **Xiaoning Tian:** Resources,

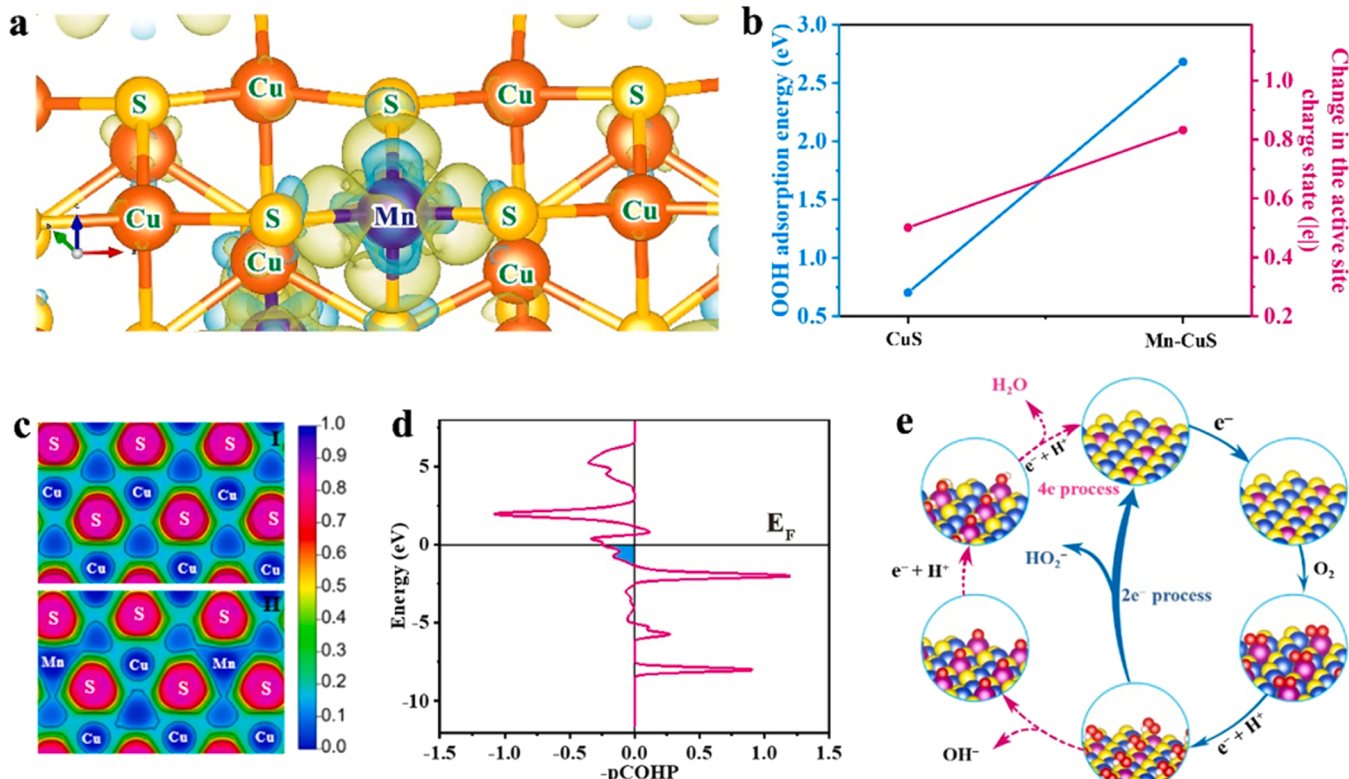


Fig. 6. (a) Charge density difference of Mn-CuS (Mn-substituted CuS). Cyan and yellow isosurfaces (+0.006Bohr⁻³) show the loss and gain of valence electrons, respectively; (b) Calculated OOH^* adsorption energies and relative charge states of the active site (metal) in CuS and Mn-CuS; (c) The ELF plot crossing the unit cell of bulk CuS (I) and Mn-CuS (II), which belongs to (001) slices; (d) COHP curves of the Mn-OOH bond for the adsorption of OOH onto the (001) surfaces of Mn-CuS. The antibonding contribution is defined as negative on the plot and the bonding contribution as positive. The black horizontal line means the Fermi level (E_F); (e) Reaction cycles of H_2O_2 production with the energetically most feasible active sites.

Validation, Writing – original draft, Writing – review & editing. **Yangjie Liu:** Writing – original draft. **Zhongyu Cai:** Conceptualization, Methodology, Resources, Formal analysis, Data curation, Writing – original draft, Writing – review & editing, Visualization, Supervision, Project administration, Funding acquisition.

Declaration of Competing Interest

The authors declare that they have no known competing financial interests or personal relationships that could have appeared to influence the work reported in this paper.

Data Availability

Data will be made available on request.

Acknowledgment

This work was financially supported by National Natural Science Foundation of China under award Nos. 22076008 (Z.C.), 52222101 (N. M.), 92163131 (N.H.), and 11975205 (Z.J.), and BUAA Faculty Research Grant under Grant Nos. ZG216S2094 (Z.C.) and ZG216S2153 (Z.C.).

Appendix A. Supporting information

Supplementary data associated with this article can be found in the online version at [doi:10.1016/j.apcatb.2023.122721](https://doi.org/10.1016/j.apcatb.2023.122721).

References

- [1] J.M. Campos-Martin, G. Blanco-Brieva, J.L.G. Fierro, Hydrogen peroxide synthesis: an outlook beyond the anthraquinone process, *Angew. Chem. Int. Ed.* 45 (2006) 6962–6984, <https://doi.org/10.1002/anie.200503779>.
- [2] C. Xia, Y. Xia, P. Zhu, L. Fan, H. Wang, Direct electrosynthesis of pure aqueous H_2O_2 solutions up to 20% by weight using a solid electrolyte, *Science* 366 (2019) 226–231, <https://doi.org/10.1126/science.aaay1844>.
- [3] S.A. Mousavi Shaegh, N.-T. Nguyen, S.M. Mousavi Ehteshami, S.H. Chan, A membraneless hydrogen peroxide fuel cell using Prussian Blue as cathode material, *Energy Environ. Sci.* 5 (2012) 8225–8228, <https://doi.org/10.1039/C2EE21806B>.
- [4] J.K. Edwards, G.J. Hutchings, Palladium and gold–palladium catalysts for the direct synthesis of hydrogen peroxide, *Angew. Chem. Int. Ed.* 47 (2008) 9192–9198, <https://doi.org/10.1002/anie.200802818>.
- [5] Y. Sun, L. Han, P. Strasser, A comparative perspective of electrochemical and photochemical approaches for catalytic H_2O_2 production, *Chem. Soc. Rev.* 49 (2020) 6605–6631, <https://doi.org/10.1039/D0CS00458H>.
- [6] S. Yang, A. Verdaguera-Casadevall, L. Arnarson, L. Silvioli, V. Čolić, R. Frydendal, J. Rossmeisl, I. Chorkendorff, I.E.L. Stephens, Toward the decentralized electrochemical production of H_2O_2 : a focus on the catalysis, *ACS Catal.* 8 (2018) 4064–4081, <https://doi.org/10.1021/acscatal.8b00217>.
- [7] A. Verdaguera-Casadevall, D. Deiana, M. Karamad, S. Siahrostami, P. Malacrida, T. W. Hansen, J. Rossmeisl, I. Chorkendorff, I.E.L. Stephens, Trends in the electrochemical synthesis of H_2O_2 : enhancing activity and selectivity by electrocatalytic site engineering, *Nano Lett.* 14 (2014) 1603–1608, <https://doi.org/10.1021/nl500037x>.
- [8] N. Wang, S. Ma, P. Zuo, J. Duan, B. Hou, Recent progress of electrochemical production of hydrogen peroxide by two-electron oxygen reduction reaction, *Adv. Sci.* 8 (2021) 2100076, <https://doi.org/10.1002/advs.202100076>.
- [9] S. Siahrostami, A. Verdaguera-Casadevall, M. Karamad, D. Deiana, P. Malacrida, B. Wickman, M. Escudero-Escribano, E.A. Paoli, R. Frydendal, T.W. Hansen, I. Chorkendorff, I.E.L. Stephens, J. Rossmeisl, Enabling direct H_2O_2 production through rational electrocatalyst design, *Nat. Mater.* 12 (2013) 1137–1143, <https://doi.org/10.1038/nmat3795>.
- [10] A.R. Zeradjanin, Is a major breakthrough in the oxygen electrocatalysis possible? *Curr. Opin. Electrochem.* 9 (2018) 214–223, <https://doi.org/10.1016/j.coelec.2018.04.006>.
- [11] K. Dong, Y. Lei, H. Zhao, J. Liang, P. Ding, Q. Liu, Z. Xu, S. Lu, Q. Li, X. Sun, Noble-metal-free electrocatalysts toward H_2O_2 production, *J. Mater. Chem. A* 8 (2020) 23123–23141, <https://doi.org/10.1039/D0TA08894C>.
- [12] Y. Bu, Y. Wang, G.-F. Han, Y. Zhao, X. Ge, F. Li, Z. Zhang, Q. Zhong, J.-B. Baek, Carbon-based electrocatalysts for efficient hydrogen peroxide production, *Adv. Mater.* 33 (2021) 2103266, <https://doi.org/10.1002/adma.202103266>.
- [13] S. Ponnada, M.S. Kjai, D.B. Gorle, R.S.C. Bose, V. Rajagopal, B. Saini, M. Kathiresan, A. Nowduri, R. Singhal, F. Marken, M.A. Kulandainathan, K. K. Nanda, R.K. Sharma, Recent status and challenges in multifunctional electrocatalysis based on 2D MXenes, *Catal. Sci. Technol.* 12 (2022) 4413–4441, <https://doi.org/10.1039/D2CY00428C>.
- [14] Y. Liu, X. Zhang, W. Zhang, X. Ge, Y. Wang, X. Zou, X. Zhou, W. Zheng, MXene-based quantum dots optimize hydrogen production via spontaneous evolution of Cl- to O-terminated surface groups, *Energy Environ. Mater.* (2022), e12438, <https://doi.org/10.1002/eem2.12438>.
- [15] X. Hu, X. Zeng, Y. Liu, J. Lu, X. Zhang, Carbon-based materials for photo- and electrocatalytic synthesis of hydrogen peroxide, *Nanoscale* 12 (2020) 16008–16027, <https://doi.org/10.1039/DONR03178J>.
- [16] X. Liu, L. Dai, Carbon-based metal-free catalysts, *Nat. Rev. Mater.* 1 (2016) 16064, <https://doi.org/10.1038/natrevmats.2016.64>.
- [17] X. Huang, W. Zhang, W. Liu, J. Zhang, M. Song, C. Zhang, J. Zhang, D. Wang, Nb2CTx MXenes functionalized Co–NC enhancing electrochemical H_2O_2 production for organics degradation, *Appl. Catal., B* 317 (2022), 121737, <https://doi.org/10.1016/j.apcatb.2022.121737>.
- [18] X. Guo, S. Lin, J. Gu, S. Zhang, Z. Chen, S. Huang, Simultaneously achieving high activity and selectivity toward two-electron O_2 electroreduction: the power of single-atom catalysts, *ACS Catal.* 9 (2019) 11042–11054, <https://doi.org/10.1021/acscatal.9b02778>.
- [19] M.B. Zakaria, C. Li, M. Pramanik, Y. Tsujimoto, M. Hu, V. Malgras, S. Tominaka, Y. Yamauchi, Nanoporous Mn-based electrocatalysts through thermal conversion of cyano-bridged coordination polymers toward ultra-high efficiency hydrogen peroxide production, *J. Mater. Chem. A* 4 (2016) 9266–9274, <https://doi.org/10.1039/C6TA01470D>.
- [20] H. Liu, X. Zhu, M. Li, Q. Tang, G. Sun, W. Yang, Single crystal (Mn,Co)3O4 octahedra for highly efficient oxygen reduction reactions, *Electrochim. Acta* 144 (2014) 31–41, <https://doi.org/10.1016/j.electacta.2014.08.087>.
- [21] M. Suk, M.W. Chung, M.H. Han, H.-S. Oh, C.H. Choi, Selective H_2O_2 production on surface-oxidized metal–nitrogen–carbon electrocatalysts, *Catal. Today* 359 (2021) 99–105, <https://doi.org/10.1016/j.cattod.2019.05.034>.
- [22] B.-Q. Li, C.-X. Zhao, J.-N. Liu, Q. Zhang, Electrosynthesis of hydrogen peroxide synergistically catalyzed by atomic Co–Nx–C sites and oxygen functional groups in noble-metal-free electrocatalysts, *Adv. Mater.* 31 (2019) 1808173, <https://doi.org/10.1002/adma.201808173>.
- [23] S. Siahrostami, S.J. Villegas, A.H. Bagherzadeh Mostaghimi, S. Back, A.B. Farimani, H. Wang, K.A. Persson, J. Montoya, A review on challenges and successes in atomic-scale design of catalysts for electrochemical synthesis of hydrogen peroxide, *ACS Catal.* 10 (2020) 7495–7511, <https://doi.org/10.1021/acscatal.0c01641>.
- [24] K. Cho, S.-H. Han, M.P. Suh, Copper–organic framework fabricated with CuS nanoparticles: synthesis, electrical conductivity, and electrocatalytic activities for oxygen reduction reaction, *Angew. Chem. Int. Ed.* 55 (2016) 15301–15305, <https://doi.org/10.1002/anie.201607271>.
- [25] M. Chandra, K. Bhunia, D. Pradhan, Controlled synthesis of CuS/TiO₂ heterostructured nanocomposites for enhanced photocatalytic hydrogen generation through water splitting, *Inorg. Chem.* 57 (2018) 4524–4533, <https://doi.org/10.1021/acs.inorgchem.8b00283>.
- [26] S.-Q. Liu, H.-R. Wen, G. Ying, Y.-W. Zhu, X.-Z. Fu, R. Sun, C.-P. Wong, Amorphous Ni(OH)₂ encounter with crystalline Cu⁺ in hollow spheres: a mesoporous nano-shelled heterostructure for hydrogen evolution electrocatalysis, *Nano Energy* 44 (2018) 7–14, <https://doi.org/10.1016/j.nano.2017.11.063>.
- [27] M.-R. Gao, Y.-F. Xu, J. Jiang, S.-H. Yu, Nanostructured metal chalcogenides: synthesis, modification, and applications in energy conversion and storage devices, *Chem. Soc. Rev.* 42 (2013) 2986–3017, <https://doi.org/10.1039/C2CS35310E>.
- [28] Y. Fang, B.Y. Guan, D. Luan, X.W. Lou, Synthesis of CuS@CoS₂ double-shelled nanoboxes with enhanced sodium storage properties, *Angew. Chem. Int. Ed.* 58 (2019) 7739–7743, <https://doi.org/10.1002/anie.201902583>.
- [29] J. Kundu, S. Khilari, K. Bhunia, D. Pradhan, Ni-Doped CuS as an efficient electrocatalyst for the oxygen evolution reaction, *Catal. Sci. Technol.* 9 (2019) 406–417, <https://doi.org/10.1039/C8CY02181C>.
- [30] Y. Jiang, P. Ni, C. Chen, Y. Lu, P. Yang, B. Kong, A. Fisher, X. Wang, Selective electrochemical H_2O_2 production through two-electron oxygen electrochemistry, *Adv. Energy Mater.* 8 (2018) 1801909, <https://doi.org/10.1002/aenm.201801909>.
- [31] H. Zhao, Z.-Y. Yuan, Design strategies of non-noble metal-based electrocatalysts for two-electron oxygen reduction to hydrogen peroxide, *ChemSusChem* 14 (2021) 1616–1633, <https://doi.org/10.1002/cssc.202100055>.
- [32] Y. Yu, G.-H. Nam, Q. He, X.-J. Wu, K. Zhang, Z. Yang, J. Chen, Q. Ma, M. Zhao, Z. Liu, F.-R. Ran, X. Wang, H. Li, X. Huang, B. Li, Q. Xiong, Q. Zhang, Z. Liu, L. Gu, Y. Du, W. Huang, H. Zhang, High phase-purity 1T'-Mo₂ and 1T'-MoSe₂ layered crystals, *Nat. Chem.* 10 (2018) 638–643, <https://doi.org/10.1038/s41557-018-0035-6>.
- [33] L. Liu, J. Wu, L. Wu, M. Ye, X. Liu, Q. Wang, S. Hou, P. Lu, L. Sun, J. Zheng, L. Xing, L. Gu, X. Jiang, L. Xie, L. Jiao, Phase-selective synthesis of 1T' MoS₂ monolayers and heterophase bilayers, *Nat. Mater.* 17 (2018) 1108–1114, <https://doi.org/10.1038/s41563-018-0187-1>.
- [34] L. Yu, B.Y. Xia, X. Wang, X.W. Lou, General formation of M–MoS₃ (M = Co, Ni) hollow structures with enhanced electrocatalytic activity for hydrogen evolution, *Adv. Mater.* 28 (2016) 92–97, <https://doi.org/10.1002/adma.201504024>.
- [35] D. Yan, Y. Li, J. Huo, R. Chen, L. Dai, S. Wang, Defect chemistry of nonprecious-metal electrocatalysts for oxygen reactions, *Adv. Mater.* 29 (2017) 1606459, <https://doi.org/10.1002/adma.201606459>.
- [36] M. Jahan, Q. Bao, K.P. Loh, Electrocatalytically active graphene–porphyrin moF composite for oxygen reduction reaction, *J. Am. Chem. Soc.* 134 (2012) 6707–6713, <https://doi.org/10.1021/ja211433h>.
- [37] Y. Sun, L. Silvioli, N.R. Sahraie, W. Ju, J. Li, A. Zitolo, S. Li, A. Bagger, L. Arnarson, X. Wang, T. Moeller, D. Bernsmeier, J. Rossmisl, F. Jaouen, P. Strasser, Activity–selectivity trends in the electrochemical production of hydrogen peroxide

over single-site metal–nitrogen–carbon catalysts, *J. Am. Chem. Soc.* 141 (2019) 12372–12381, <https://doi.org/10.1021/jacs.9b05576>.

[38] W. Fan, B. Zhang, X. Wang, W. Ma, D. Li, Z. Wang, M. Dupuis, J. Shi, S. Liao, C. Li, Efficient hydrogen peroxide synthesis by metal-free polyterthiophene via photoelectrocatalytic dioxygen reduction, *Energy Environ. Sci.* 13 (2020) 238–245, <https://doi.org/10.1039/C9EE02247C>.

[39] H.W. Kim, M.B. Ross, N. Kornienko, L. Zhang, J. Guo, P. Yang, B.D. McCloskey, Efficient hydrogen peroxide generation using reduced graphene oxide-based oxygen reduction electrocatalysts, *Nat. Catal.* 1 (2018) 282–290, <https://doi.org/10.1038/s41929-018-0044-2>.

[40] Z. Lu, G. Chen, S. Siahrostami, Z. Chen, K. Liu, J. Xie, L. Liao, T. Wu, D. Lin, Y. Liu, T.F. Jaramillo, J.K. Nørskov, Y. Cui, High-efficiency oxygen reduction to hydrogen peroxide catalysed by oxidized carbon materials, *Nat. Catal.* 1 (2018) 156–162, <https://doi.org/10.1038/s41929-017-0017-x>.

[41] E. Jung, H. Shin, B.-H. Lee, V. Efremov, S. Lee, H.S. Lee, J. Kim, W. Hooch Antink, S. Park, K.-S. Lee, S.-P. Cho, J.S. Yoo, Y.-E. Sung, T. Hyeon, Atomic-level tuning of Co–N–C catalyst for high-performance electrochemical H_2O_2 production, *Nat. Mater.* 19 (2020) 436–442, <https://doi.org/10.1038/s41563-019-0571-5>.

[42] P.E. Blöchl, Projector augmented-wave method, *Phys. Rev. B* 50 (1994) 17953–17979, <https://doi.org/10.1103/PhysRevB.50.17953>.

[43] J. Hafner, Ab-initio simulations of materials using VASP: density-functional theory and beyond, *J. Comput. Chem.* 29 (2008) 2044–2078, <https://doi.org/10.1002/jcc.21057>.

[44] J.P. Perdew, K. Burke, M. Ernzerhof, Generalized gradient approximation made simple, *Phys. Rev. Lett.* 77 (1996) 3865–3868, <https://doi.org/10.1103/PhysRevLett.77.3865>.

[45] M.J. Gillan, D. Alfe, A. Michaelides, Perspective: how good is DFT for water?, *J. Chem. Phys.* 144 (2016) 130901 <https://doi.org/10.1063/1.4944633>.

[46] V.L. Deringer, A.L. Tchougréeff, R. Dronkowski, Crystal orbital hamilton population (COHP) analysis as projected from plane-wave basis sets, *J. Phys. Chem. A* 115 (2011) 5461–5466, <https://doi.org/10.1021/jp202489s>.

[47] R. Dronkowski, P.E. Blöchl, Crystal orbital Hamilton populations (COHP): energy-resolved visualization of chemical bonding in solids based on density-functional calculations, *J. Phys. Chem.* 97 (1993) 8617–8624, <https://doi.org/10.1021/j100135a014>.

[48] S. Maintz, V.L. Deringer, A.L. Tchougréeff, R. Dronkowski, LOBSTER: A tool to extract chemical bonding from plane-wave based DFT, *J. Comput. Chem.* 37 (2016) 1030–1035, <https://doi.org/10.1002/jcc.24300>.

[49] H. Liu, Z. Guo, X. Wang, J. Hao, J. Lian, CuS/MnS composite hexagonal nanosheet clusters: synthesis and enhanced pseudocapacitive properties, *Electrochim. Acta* 271 (2018) 425–432, <https://doi.org/10.1016/j.electacta.2018.03.048>.

[50] Y. Chen, J. Li, Z. Lei, Y. Huo, L. Yang, S. Zeng, H. Ding, Y. Qin, Y. Jie, F. Huang, Q. Li, J. Zhu, R. Cao, G. Zhang, S. Jiao, D. Xu, Hollow CuS nanoboxes as Li-free cathode for high-rate and long-life lithium metal batteries, *Adv. Energy Mater.* 10 (2020) 1903401, <https://doi.org/10.1002/aenm.201903401>.

[51] L. Zhou, J. Feng, B. Qiu, Y. Zhou, J. Lei, M. Xing, L. Wang, Y. Zhou, Y. Liu, J. Zhang, Ultrathin g-C₃N₄ nanosheet with hierarchical pores and desirable energy band for highly efficient H_2O_2 production, *Appl. Catal. B* 267 (2020), 118396, <https://doi.org/10.1016/j.apcatb.2019.118396>.

[52] J. Qu, Y. Ge, B. Zu, Y. Li, X. Dou, Transition-metal-doped p-Type ZnO nanoparticle-based sensory array for instant discrimination of explosive vapors, *Small* 12 (2016) 1369–1377, <https://doi.org/10.1002/smll.201503131>.

[53] S. Chen, Z. Chen, S. Siahrostami, T.R. Kim, D. Nordlund, D. Sokaras, S. Nowak, J. W.F. To, D. Higgins, R. Sinclair, J.K. Nørskov, T.F. Jaramillo, Z. Bao, Defective carbon-based materials for the electrochemical synthesis of hydrogen peroxide, *ACS Sustain. Chem. Eng.* 6 (2018) 311–317, <https://doi.org/10.1021/acssuschemeng.7b02517>.

[54] S.T. Ochsenbein, Y. Feng, K.M. Whitaker, E. Badaeva, W.K. Liu, X. Li, D.R. Gamelin, Charge-controlled magnetism in colloidal doped semiconductor nanocrystals, *Nat. Nanotechnol.* 4 (2009) 681–687, <https://doi.org/10.1038/nano.2009.221>.

[55] Q. Jin, N. Liu, C. Dai, R. Xu, B. Wu, G. Yu, B. Chen, Y. Du, H₂-directing strategy on in situ synthesis of Co-MoS₂ with highly expanded interlayer for elegant HER activity and its mechanism, *Adv. Energy Mater.* 10 (2020) 2000291, <https://doi.org/10.1002/aenm.202000291>.

[56] Q. Gong, L. Cheng, C. Liu, M. Zhang, Q. Feng, H. Ye, M. Zeng, L. Xie, Z. Liu, Y. Li, Ultrathin MoS_{2(1-x)Se₂} alloy nanoflakes for electrocatalytic hydrogen evolution reaction, *ACS Catal.* 5 (2015) 2213–2219, <https://doi.org/10.1021/cs501970w>.

[57] X. Liu, J. Wang, L. Yue, B. Xin, S. Chen, J. Dai, R. Wang, Y. Wang, Biosynthesis of high-purity γ -MnS nanoparticle by newly isolated Clostridiaceae sp. and its properties characterization, *Bioprocess Biosyst. Eng.* 38 (2015) 219–227, <https://doi.org/10.1007/s00449-014-1261-y>.

[58] F. Xiong, Y. Fan, S. Tan, L. Zhou, Y. Xu, C. Pei, Q. An, L. Mai, Magnesium storage performance and mechanism of CuS cathode, *Nano Energy* 47 (2018) 210–216, <https://doi.org/10.1016/j.nanoen.2018.02.060>.

[59] A. Morales-García, A.L. Soares Jr., E.C. Dos Santos, H.A. de Abreu, H.A. Duarte, First-principles calculations and electron density topological analysis of covellite (CuS), *J. Phys. Chem. A* 118 (2014) 5823–5831, <https://doi.org/10.1021/jp4114706>.

[60] V. Ragupathi, P. Panigrahi, N. Ganapathi Subramanian, g-C₃N₄ doped MnS as high performance electrode material for supercapacitor application, *Mater. Lett.* 246 (2019) 88–91, <https://doi.org/10.1016/j.matlet.2019.03.054>.

[61] Z. Yang, T. Chen, C. Wu, J. Qu, Z. Wu, X. Guo, B. Zhong, H. Liu, S. Dou, Interpreting abnormal charge-discharge plateau migration in Cu_xS during long-term cycling, *ACS Appl. Mater. Interfaces* 11 (2019) 3961–3970, <https://doi.org/10.1021/acsami.8b18864>.

[62] H. Lei, G. Yang, X. Zheng, Z.-G. Zhang, C. Chen, J. Ma, Y. Guo, Z. Chen, P. Qin, Y. Li, G. Fang, Incorporation of high-mobility and room-temperature-deposited cuxs as a hole transport layer for efficient and stable organo-lead halide perovskite solar cells, *Sol. RRL* 1 (2017) 1700038, <https://doi.org/10.1002/solr.201700038>.

[63] X. Chen, H. Abdullah, D.-H. Kuo, CuMnOS nanoflowers with different Cu⁺/Cu²⁺ Ratios for the CO₂-to-CH₃OH and the CH₃OH-to-H₂ redox reactions, *Sci. Rep.* 7 (2017) 41194, <https://doi.org/10.1038/srep41194>.

[64] Y. Ma, Y. Ma, G.-T. Kim, T. Diemant, R.J. Behm, D. Geiger, U. Kaiser, A. Varzi, S. Passerini, Superior lithium storage capacity of α -MnS nanoparticles embedded in S-doped carbonaceous mesoporous frameworks, *Adv. Energy Mater.* 9 (2019) 1902077, <https://doi.org/10.1002/aenm.201902077>.

[65] L.Z. Pei, J.F. Wang, X.X. Tao, S.B. Wang, Y.P. Dong, C.G. Fan, Q.-F. Zhang, Synthesis of CuS and Cu_{1-x}Fe_{1.5}S_x crystals and their electrochemical properties, *Mater. Charact.* 62 (2011) 354–359, <https://doi.org/10.1016/j.matchar.2011.01.001>.

[66] D. Geetha, J.W. Brown, P.S. Ramesh, S. Podili, Nanoporous transition metal sulfide (Cd–CuS) active electrode material for electrochemical energy storage device, *J. Mater. Sci.: Mater. Electron.* 31 (2020) 983–993, <https://doi.org/10.1007/s10854-019-02609-x>.

[67] R. Shen, W. Chen, Q. Peng, S. Lu, L. Zheng, X. Cao, Y. Wang, W. Zhu, J. Zhang, Z. Zhuang, C. Chen, D. Wang, Y. Li, High-concentration single atomic Pt sites on hollow Cu_xS for selective O₂ reduction to H₂O₂ in acid solution, *Chem* 5 (2019) 2099–2110, <https://doi.org/10.1016/j.chempr.2019.04.024>.

[68] A. Byeon, J. Cho, J.M. Kim, K.H. Chae, H.-Y. Park, S.W. Hong, H.C. Ham, S.W. Lee, K.R. Yoon, J.Y. Kim, High-yield electrochemical hydrogen peroxide production from an enhanced two-electron oxygen reduction pathway by mesoporous nitrogen-doped carbon and manganese hybrid electrocatalysts, *Nanoscale Horiz.* 5 (2020) 832–838, <https://doi.org/10.1039/C9NH00783K>.